

Integrated platform to assess seismic resilience at the community level

Original

Integrated platform to assess seismic resilience at the community level / Marasco, S.; Cardoni, A.; Zamani Noori, A.; Kammouh, O.; Domaneschi, M.; Cimellaro, G. P.. - In: SUSTAINABLE CITIES AND SOCIETY. - ISSN 2210-6707. - ELETTRONICO. - 64:(2021), pp. 1-20. [10.1016/j.scs.2020.102506]

Availability:

This version is available at: 11583/2857052 since: 2020-12-23T01:58:51Z

Publisher:

Elsevier

Published

DOI:10.1016/j.scs.2020.102506

Terms of use:

This article is made available under terms and conditions as specified in the corresponding bibliographic description in the repository

Publisher copyright

Elsevier postprint/Author's Accepted Manuscript

© 2021. This manuscript version is made available under the CC-BY-NC-ND 4.0 license
<http://creativecommons.org/licenses/by-nc-nd/4.0/>. The final authenticated version is available online at:
<http://dx.doi.org/10.1016/j.scs.2020.102506>

(Article begins on next page)

44 Understanding the vulnerability of critical infrastructures is of paramount importance as it
45 allows to properly predict community resilience, which is defined as the ability of a system to
46 respond and recover from disaster (Cimellaro et al., 2016; Cutter et al., 2008). Among all
47 definitions of resilience, (Walker & Salt, 2006) define resilient systems as “sustaining
48 ecosystems and people in a changing world”, therefore resilience is intertwined with
49 sustainability. Resilience can be considered as one of the indicators of sustainability as being
50 resilient is essential for being sustainable (G. P. Cimellaro, 2016).

51 Current practices of infrastructure modeling incorporate both facilities (housing, commercial,
52 and cultural facilities) and lifelines (hospitals, transportation systems, power and
53 communication networks, water distribution networks, etc.) (Renschler et al., 2010). However,
54 there is still a lack of tools and methods to assess resilience at the urban level (Ribeiro &
55 Gonçalves, 2019).

56 The first step towards large-scale urban simulations is the development of standards and
57 metrics that enable decision-makers to quantify resilience. An indicator-based framework for
58 measuring urban community resilience was introduced by Kammouh et al. (2019). The
59 framework, namely *PEOPLES*, captures the overall resilience of communities considering
60 different aspects/layers, i.e., population, environmental and ecosystem, organized
61 governmental services, physical infrastructures, lifestyle, economic development, and social
62 capital. Karakoc et al. (2020) proposed an important measure that is derived by social aspects
63 of resilience to identify the most critical components that have the largest impact on the
64 performance of interdependent networks. A hybrid simulation framework was suggested by
65 Hwang et al. (2016) to plan immediate recovery measures for the regional facilities in the

66 aftermath of a disaster combining system dynamic approaches with discrete-event simulations.
67 More detailed indicator-based models have been developed for single infrastructures typical of
68 modern communities. For instance, Balaei et al. (2020) identified indicators to quantify the
69 robustness and consequently the resilience of water supply systems, which are essential in the
70 aftermath of a disaster.

71 The interaction among critical infrastructures needs to be examined to correctly model and
72 comprehensively analyze the community system. A modeling and simulation framework was
73 developed by Dudenhoeffer et al. (2006) to simulate the urban infrastructure interdependencies
74 given a flood event. Infrastructures were modeled as a network consisting of nodes and edges,
75 while interdependencies were defined as direct links between infrastructures' components.
76 Focusing on system interdependencies and related cascading effects, Guidotti et al. (2016)
77 investigated the effects of the seismic damage of an electric power network on a water
78 distribution network while Domaneschi et al. (2019) focused on the interdependency between
79 seismic damage of masonry buildings and transportation networks. In addition, a recent study
80 showed the importance of considering the pre-event conditions of interdependent stormwater
81 drainage system and road transportation network (Yang et al., 2019).

82 Recent years have seen a rise in the development of integrated platforms to quantify the
83 resilience of infrastructure systems. In their research, Repetto et al. (2017) provided tools for
84 real-time monitoring of seaports which can have a highly positive impact on improving the
85 resilience of coastal urban communities. Different applications can be found for different
86 scenarios and hazards. Among others, a conceptual integrated framework (Martí, 2014) was
87 proposed to plan and coordinate the response of multiple infrastructures during disasters.

88 Borgdorff et al. (2015) developed a software tool (SIM-CITY) to predict complex urban
89 dynamics to coordinate emergency services and urban planners. An example of a Virtual
90 Geographic Environment (VGE)-based simulation framework for flood disaster management
91 was presented by Ding et al. (2014), while a community-driven project named Global
92 Earthquake Model (GEM) (Crowley et al., 2013) simulates earthquake risks. The main goal of
93 the GEM foundation is to define standards and collect best practices related to seismic hazard
94 and risk assessment methodologies, with a focus on data collection and storage. Besides,
95 seismic vulnerability through empirical, analytical, and expert opinion was addressed by Porter
96 et al. (2012), while an open-source software named the OpenQuake (Silva et al., 2014) was
97 developed to evaluate human or economic losses.

98 Although previous studies have tackled disaster community modeling and simulation, the
99 integration of all computing resources into a unified platform remains a challenge. An
100 integrated platform would provide a more effective problem-solving approach that is useful to
101 assist the decision support system. This poses several practical challenges in enabling different
102 simulators to interact and in organizing the information system flow for a standardized output.

103 The main objective of this work is to develop an integrated platform to assess seismic
104 resilience at the community level. With this aim, new methods and computational procedures
105 are proposed. These methods are implemented in a new software tool that assesses the
106 vulnerability of critical infrastructures in large-scale urban areas. Besides, innovative physical
107 interdependency models have been implemented in the platform. As a testbed, a virtual city
108 that mimics a typical Italian building stock is designed. The information of the physical systems
109 (i.e. buildings, transportation, power, water networks) is collected in the form of a machine-

110 readable database. The designed testbed is used throughout the manuscript to explain the
111 different methodologies introduced in this paper; thus, there will not be a separate section
112 dedicated to the methodologies.

113 The entire analysis is controlled in a Python-based environment implementing a parallel
114 computing workflow. The developed software comprises different Python classes that include
115 all necessary algorithms to assess the building portfolio damage and model the physical
116 interdependencies within and across the networks. The software tool includes visualization
117 methods that convert the numerical results into easy-to-interpret figures which can be crucial
118 for decision-makers. Resilience and interdependency analyses, which this paper is centered
119 around, help decision-makers to identify vulnerable structures and infrastructure prior to the
120 event so they can develop sustainable technologies for preparedness and reconstruction.

121 The rest of the paper is organized as follows. Section 2 gives an overview of the proposed
122 hybrid community model. Section 3 presents the details for modeling and simulating the
123 building portfolio. Section 4 describes the methods used for modeling the road infrastructure
124 network and for analyzing its interdependency with the building stock. Sections 5 and 6 deal
125 with the power system and water distribution network, respectively. In section 7, the agent-
126 based model used to simulate the socio-technical network is introduced. Section 8 presents an
127 application of the entire computational procedure considering different seismic scenarios to
128 demonstrate the platform's features and functionality. Finally, conclusions are drawn in Section
129 9.

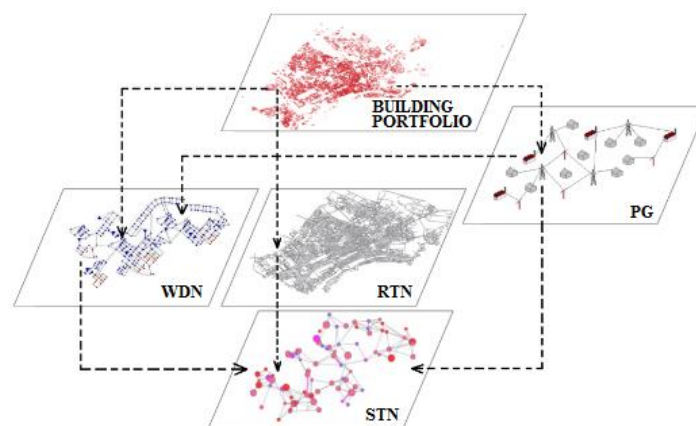
130

2. HYBRID COMMUNITY MODEL

131 Community vulnerability modeling is multi-layered as it considers the responses of different
132 infrastructures and social networks, including their interdependencies (Pamungkas et al.,
133 2014). Common approaches can be grouped into six types: empirical, agent-based, system
134 dynamics, economic theory-based, network, and others (Ouyang, 2014). Empirical approaches
135 analyze the system's components according to historical disaster data. In agent-based
136 approaches, the system is considered as adaptive and its complex behavior is described as the
137 interaction of autonomous agents (Cimellaro et al., 2017). System dynamic approaches attempt
138 to model the evolutionary behavior of interdependent infrastructures by capturing causes and
139 effects under an external impact. On the other hand, network-based approaches model each
140 infrastructure combining nodes and links, while the interdependencies among infrastructures
141 are defined using interlinks. Finally, economic theory-based approaches focus on market rules
142 to model interdependencies. Other approaches include Bayesian networks, hierarchical
143 methods, and hybrid models. The latter result from a combination of two or more traditional
144 methods (Kammouh, Noori, et al., 2018).

145 In this work, a hybrid model is proposed to couple Network Models (NMs), which are used
146 to analyze the physical infrastructures, with Agent-Based Models (ABMs) to simulate the
147 socio-technical networks (emergency rescue services, firefighters, etc.). It is applied to a virtual
148 city named *Ideal City*, which is envisioned as being representative of a typical European urban
149 area and it is inspired by the city of Turin in Italy. Its building portfolio comprises four different
150 sectors including housing (residential building, hotel, shelter), education (school, university,
151 library), business (shopping centers, retail stores, heavy industries), and public services
152 (hospital, police station, churches, airport, etc.). Figure 1 schematically shows the hybrid multi-

153 layered model of *Ideal City* and the interdependencies among the networks. Four lifelines
154 supporting the community's demands are modeled: (i) the Road Transportation Network
155 (RTN), (ii) the Water Distribution Network (WDN), (iii) the Power Grid (PG), and (iv) the
156 Socio-Technical Network (STN). The proposed hybrid model takes into account also cascading
157 effects between the building damage and the RTN, the PG, the WDN, and the STN in the
158 aftermath of an earthquake.



159

160 **Figure 1.** Hybrid multi-layered model and interdependencies (dashed arrows).

161 The dashed lines refer to the interdependencies between layers that have been modeled in the
162 proposed platform. The damage experienced by the building portfolio is considered as the
163 trigger event inducing an additional loss of functionality in all the remaining networks (RTN,
164 WDN, PG, and STN). Moreover, the functionality of WDN is dependent on the PG due to the
165 presence of pumps and electric valves. The functionality of all the considered physical
166 networks affects the STN response (e.g. emergency rescue and evacuation, human behavior).

167

3. MODELING THE BUILDING PORTFOLIO

168 Performing urban large-scale simulations, some generalizations and simplifications on the
169 building portfolio are necessary to overcome the lack of data and to limit the computational

170 workflow. Therefore, a *surrogate* model to describe the lateral behavior of each building is
171 herein adopted by considering the relationship between its base shear and top horizontal
172 displacement (Marasco et al. (2017); Noori et al. (2017)). The lateral stiffness properties are
173 modeled through a parameterized backbone curve, where the post-elastic line is characterized
174 by progressive decreasing stiffness, while hysteresis is accounted through the Takeda model
175 (Takeda et al., 1970).

176 **3.1 Building exposure database**

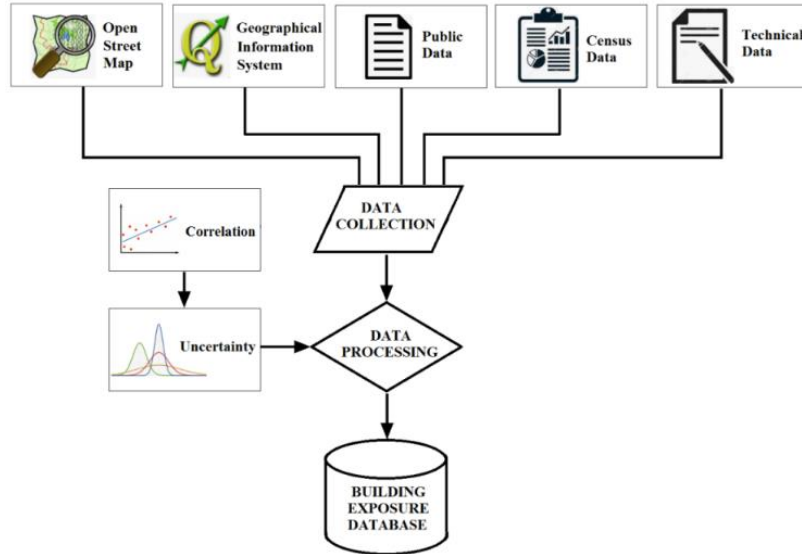
177 An essential advantage of the *surrogate* model is the limited computational effort it requires
178 with respect to a more refined finite element model, providing a significant benefit for large-
179 scale urban simulations. However, it presents several practical challenges because detailed
180 information about each building is generally not available. To overcome this issue, different
181 methods have been proposed to classify the building stock based on their typical characteristics
182 (Crowley et al., 2013; Lu & Guan, 2017). Although rapid, these methods are not so accurate
183 because they could give similar results for buildings with different structural characteristics.

184 The approach proposed herein can collect data from different public and accessible sources.
185 Based on the building stock of the city of Turin, general geometrical parameters (e.g., footprint
186 area and total height) have been obtained from OpenStreetMap (Haklay & Weber, 2008), while
187 more detailed information (e.g., number of stories, year of construction) have been found in
188 Geographical Information Systems (Maguire, 1991). Besides, further public information
189 (provided by Municipality or other authorities), census data (provided by National or regional
190 Statistical Institute, ISTAT (2016)), and other technical information (e.g. real estate data,
191 design guidance) have been exploited to increase the level of knowledge.

192 Data analysis has been performed to identify common patterns; e.g. building's age has been
193 correlated with the adopted design methods and parameters (e.g. load combinations and
194 material strength classes), which has been used to estimate the minimum required geometrical
195 and mechanical characteristics of the structural components. However, this procedure may lead
196 to discrepancies with real data. Therefore, uncertainties characterization has been introduced
197 to face the statistical nature of data, considering the buildings' parameters as normally
198 distributed Random Variables (RVs).

199 Correlation among the different variables used in the analysis may also exist. In this study,
200 the correlation between the reinforcement percentage and the characteristic reinforcing bar
201 yield strength has been considered according to the Probabilistic Model Code (Vrouwenvelder
202 & Faber, 2001). Also, a correlation between characteristic compressive strength and the elastic
203 modulus of the concrete (Mirza & MacGregor, 1979) has been considered assuming a
204 correlation coefficient of 0.8.

205 The flowchart of the data analysis is shown in Figure 2. Sources are illustrated on the top of
206 the scheme as they contribute to the data collection phase. Then, correlations among the
207 variables are considered in the data processing phase, and, finally, the processed data are stored
208 in a standard format to create a comprehensive building exposure database.



209

210

Figure 2. Flowchart of data analysis.

211 **3.2 Backbone curve estimation**

212 Each building is modeled as Multi-Degree-Of-Freedom (MDOF), which is subjected to a
 213 monotonically increasing lateral force distribution proportional to its fundamental mode.
 214 Elastic parameters are identified by the values of base shear and top displacement that cause
 215 the yield of the weakest column. Post-elastic parameters are assessed based on the upper-bound
 216 theorem of limit analysis and the equal energy rule (Marasco et al., 2017). These parameters
 217 allow to define a backbone curve representative of an equivalent Single-Degree-Of-Freedom
 218 (SDOF) model for each building. Four-point and three-point parametrized backbone curves are
 219 adopted for RC and masonry buildings, respectively.

220 All building's parameters that are significant to predicting the global structural capacity are
 221 assumed lognormally distributed RVs. Each statistical distribution is represented by the median
 222 (μ) and dispersion value (σ). The latter is based on the completeness of the quality and
 223 confidence associated with the building parameter that depends on its level of knowledge. In

224 the proposed methodology, three classes of building parameters are identified that are:
 225 mechanical-based (M), geometrical-based (G), and construction-based (C). For each class, a
 226 certain standard deviation has been set based on the building archetype and year of construction
 227 (Table 1).

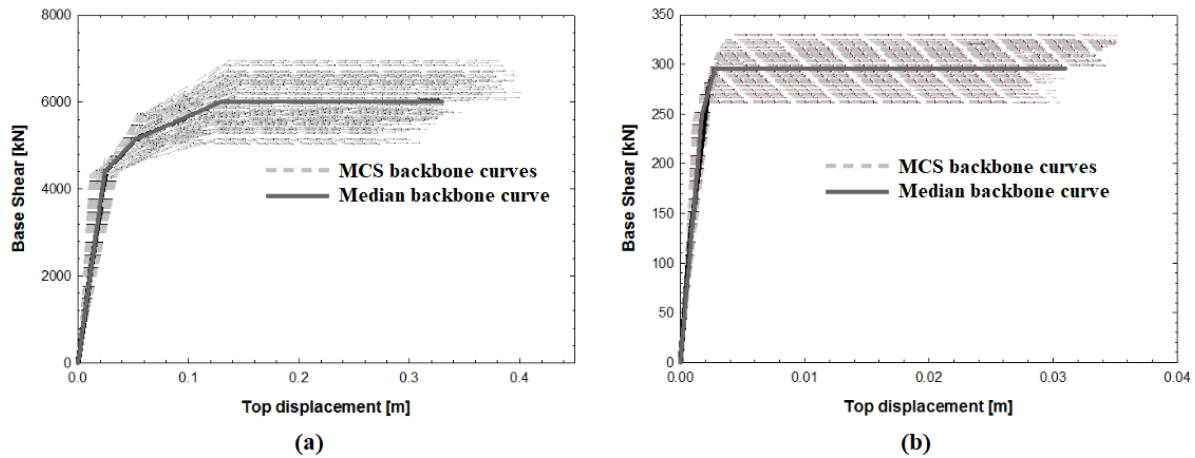
228 **Table 1.** Standard deviations associated with the mechanical, geometrical, and
 229 construction-based parameters for RC and masonry buildings based on the year of
 230 construction.

		Year of construction					
		< 1916	1916-1937	1938-1974	1975-1996	1996-2008	> 2008
RC	σ_G/μ_G	0.20	0.18	0.16	0.13	0.1	0.08
	σ_C/μ_C	0.25	0.22	0.20	0.18	0.15	0.10
	σ_M/μ_M	0.20					
Masonry	σ_G/μ_G	0.25	0.22	0.2	0.17	0.13	0.10
	σ_C/μ_C	0.28	0.26	0.24	0.22	0.20	0.18
	σ_M/μ_M	0.25					

231
 232 The standard deviation values are higher for old buildings since some of the building
 233 information lack of precision. Furthermore, a larger standard deviation is found for masonry
 234 buildings. The mechanical parameters refer to the compressive and tensile strength and elastic
 235 modulus of the constitute materials (concrete, bricks, stones, steel rebar), while the geometrical
 236 parameters are represented by the dimensions of the structural components (e.g. span length,
 237 cross-section width and depth, percentage of reinforcement). Finally, the construction-based
 238 parameters comprise all those variables that affect the building design such as the vertical and
 239 horizontal loads and the type of deck and external walls. The building data collection has been
 240 discussed in detail in the previous section.

241 The backbone curve is computed for each single building by varying its parameter through
 242 Monte Carlo Simulation (MCS) in the range $\mu \pm \sigma$. The iterative process ends when the output

243 dataset is consistent and provides a stable estimate of the median backbone curve which
244 represents the global building's capacity. As 7-story RC and 4-story masonry buildings built
245 in 1930 and 1978, respectively have been considered. The estimated median backbone curve
246 for the RC and masonry buildings have been illustrated in Figure 3.



248 **Figure 3.** Backbone curves obtained through MCS and estimated median backbone curve
249 for (a) RC and (b) masonry buildings.
250

251 3.3 Nonlinear time history analyses

252 Structural analyses have been carried out through the finite element code OpenSees (Mazzoni
253 et al., 2006). Recent advances have been introduced by Zhu et al. (2018) to offer multi-
254 interpreter capabilities resulting in the release of an “OpenSeesPy” library in Python. It has
255 been used to implement the *surrogate* model and to perform the nonlinear time history
256 analyses.

257 Each building has been modeled as “ZeroLength” element through two overlapped nodes.
258 Initial stiffness and proportional damping corresponding to the median backbone curve are
259 assigned to each element in both horizontal directions. Uniaxial “MultiLinear” material is
260 employed to simulate the force deformation relationship, while the Takeda model is adopted

261 to consider the hysteresis. Seismic input consists of a pair of time histories (in both horizontal
262 directions) applied at each element's location.

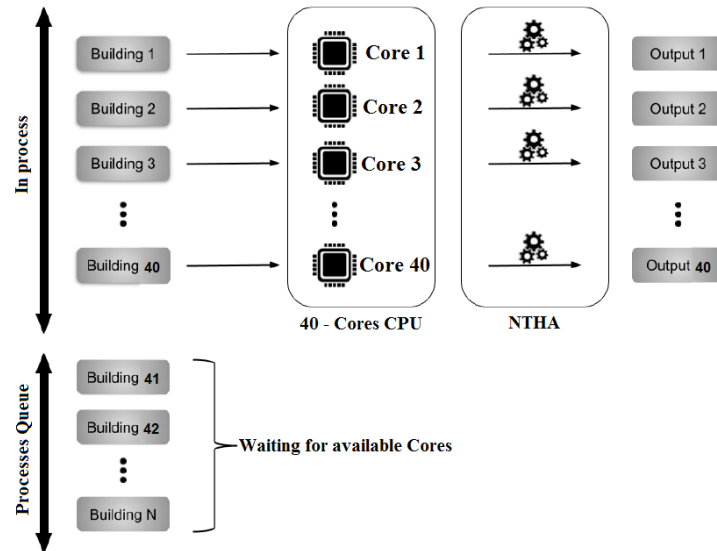
263 A simplified seismic scenario is assumed by defining epicenter location, moment magnitude,
264 and time history recorded in the epicenter. Seismic inputs at any building locations are
265 estimated based on Ambraseys' ground motion model (Ambraseys et al., 1996), while
266 frequency changing is neglected. Therefore, nonlinear time history analyses are performed and
267 the maximum top displacements of each element are computed.

268 **3.4 Multiprocessing computation**

269 Advancements in computer knowledge and architecture have led to the development of
270 algorithms that can speed up the entire computational process through parallelization
271 techniques. In parallel and distributed systems, Graphics Processing Unit (GPU) or Central
272 Processing Unit (CPU) solvers can be adopted. GPU solvers exploit the high computation
273 power of NVIDIA CUDA (Kirk, 2007) to significantly decrease the simulation time.
274 Numerical GPU algorithms can be substantially accelerated as long as the algorithms map well
275 to the specific hardware's features. For limited bandwidth problems that do not aim to the
276 solution of a large complex matrix, the GPU solution might not be optimal because it causes
277 poor or negative speedups (Ament et al., 2010). Thus, CPU-solvers may be adopted using
278 parallel programming based on *threading* and *multiprocessing* processes. The first process
279 consists of breaking the process within different parts while running the tasks that have access
280 to the same memory areas. Instead, multiprocessing consists of submitting multiple processes
281 independently to separate memory locations. The main advantage of multiprocessing is that it
282 avoids conflicts in case the processors are assessing the same memory location at the same

283 time; therefore, it is appropriate for distributed memory systems with several CPU processors
284 (e.g. supercomputers).

285 Given the considerations above, in the present study, the multiprocessing Python standard
286 library has been used. The nonlinear time history analysis of each building has been assigned
287 to different memory locations (Figure 4). A Rack Server with no. 2 Intel Xeon (E5-2698 v4
288 2.2GHz, 50MB Cache) and 256 GB RAM (8x32GB DDR4, 2400MHz) has been employed in
289 this study. A schematic representation of the procedure used to speed up the processes is shown
290 in Figure 4.



291

292

Figure 4. Multiprocessing scheme.

293

294

295

296

4. ROAD TRANSPORTATION NETWORK (RTN)

297 Road infrastructure connectivity within and among communities is essential to provide
298 services and to forward social and economic growth. This topic has inspired several studies
299 that developed different tools to investigate properties of large-scale transportation networks,
300 from Python packages like NetworkX (Hagberg et al., 2008) to open source software such as
301 Gephi (Bastian et al., 2009). Graph theory principles are certainly one of the most frequent
302 tools in this field due to their simplicity and effectiveness to solve problems related to routing,
303 traffic, minimum cost flow, etc.

304 *Ideal City's* road transportation network (RTN) has been modeled as an undirected graph G
305 (each path can be passed through in both directions) that consists of 14,239 nodes (N),
306 representing the road's intersections, and 18,798 edges (E), i.e. the links. Despite road maps are
307 directed graphs, as streets have a certain directionality, the choice of modeling the system as
308 an undirected graph has been followed because, in emergency conditions, directionality is not
309 respected to give priority to evacuation and rescue operations.

310 Theoretically, the network has been described with an $N \times N$ adjacency matrix A . The
311 elements inside A can be either 1 or 0. If $a_{i,j} = 1$, it means that node i and node j are connected,
312 while $a_{i,j} = 0$ means that nodes i and j are disconnected. Since the graph is not directed, the
313 resulting adjacency matrix is symmetric. The adjacency matrix allows computing many
314 network parameters and quickly modifying the topology of the network, e.g. when roads are
315 unavailable. An important global metric of graphs is the *average vertex degree* ($\langle vd \rangle$), which
316 indicates how many edges cross a given node (Equation (1)).

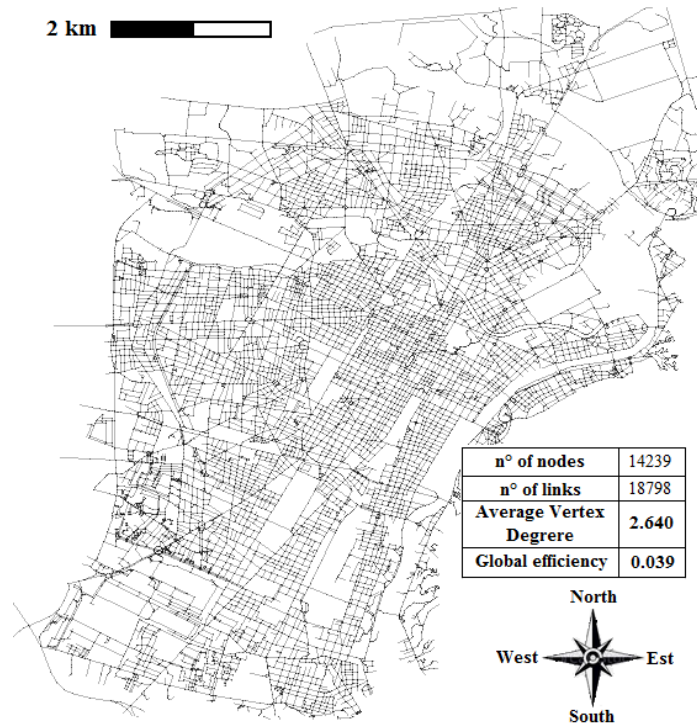
$$317 \quad \langle vd \rangle = \frac{1}{N} \sum_{i \in N} \sum_{j \in N} a_{ij} \quad (1)$$

318 In the case of an undirected graph, edges crossing a node should be considered only once,
319 thus the adjacency matrix becomes triangular.

320 *Global efficiency* is another measure of network performance that was introduced by Latora
321 and Marchiori (2001). It is defined as the average of the number of edges $d_{(i,j)}$ in the shortest
322 path between nodes i and j (Equation (2)):

$$E_{glob} = \frac{1}{N(N-1)/2} \cdot \sum_{i \neq j} \frac{1}{d_{(i,j)}} \quad (2)$$

324 The plan view of the RTN with its main properties is shown in Figure 5.



325

326

Figure 5. *Ideal City's* RTN plan view.

327 **4.1 Interdependency between buildings and RTN**

328 The interdependency between buildings and the RTN following an earthquake is caused by
329 the amount of the debris generated from the buildings' damage. To assess the amount of

330 generated debris, pictures collections by reconnaissance groups in the aftermath of worldwide
331 seismic events have been used. These collections belong to publicly available databases: the
332 Earthquake Engineering Research Institute clearinghouse and collection of case studies
333 (EERI), the Geotechnical Extreme Events Reconnaissance (GEER), and the Digital
334 Environment for Enabling Data-Driven Science (DEEDS) ones. Despite that these valuable
335 sources contain thousands of images, only a small percentage clearly shows the amount of
336 generated debris that can be measured. So after visual inspection, a database of 195 pictures
337 has been selected.

338 Each selected picture shows a building suffering a partial or complete collapse after a seismic
339 event. In total, 14 different earthquakes on different world regions have been considered, i.e.,
340 Central Italy (38 pictures), Cephalonia (6 pictures), South Napa Valley (6 pictures),
341 Christchurch (9 pictures), Ecuador (32 pictures), Nepal (38 pictures), India (6 pictures), Loma
342 Prieta (5 pictures), Central Mexico (20 pictures), North Iran (1 picture), Northridge (2 pictures),
343 Armenia (5 pictures), Taiwan (26 pictures), Turkey (1 picture).

344 In the first step, the following information has been collected: (i) the earthquake magnitude,
345 (ii) the epicentral distance, and (iii) the year of construction, (iv) the building archetype, (v) the
346 building height and (vi) the number of stories. Then, each picture has been visually inspected
347 to identify objects, such as vehicles, whose dimensions can be estimated. Starting from these
348 reference measures, the extension of the debris with acceptable accuracy has been evaluated
349 (Figure 6). Let P be the dimension of a reference object and p the debris' extension measured
350 in pixel (px). Let D and d be the corresponding measures in m of the reference object and the
351 debris extension, respectively. The debris extension d can be computed using

352 Equation (3).

353
$$d = p \cdot \frac{D}{P} \quad (3)$$

354 Then d is normalized by the building height to reduce its variance, allowing an easier
355 comparison across different models.



356

357 **Figure 6.** Example of debris extension evaluation.

358

359 Then, two machine learning (ML) algorithms have been considered: Random Forest (RF),
360 and k-Nearest Neighbors (KNN) algorithm (Liaw and Wiener (2002), Piegl and Tiller (2002)).

361 The KNN algorithm predicts a new data point starting from the closest data in the training

362 datasets, i.e. its “nearest neighbors” (Ni & Nguyen, 2009). Where ‘k’ stands for how many

363 samples are used to evaluate the prediction. An RF, instead, is essentially a collection of

364 randomized decision trees (Yao et al., 2011). The idea behind RFs is that multiple trees might

365 reduce the problem of overfitting with respect to a single decision tree. There are two ways in

366 which the trees in a random forest are randomized: by selecting the data points used to build a

367 tree and by selecting the features in each split test.

368 Both selected algorithms have been tuned to obtain the optimal result and accuracy. In the
369 KNR algorithm, the tuned parameter is the number of neighbors taken into consideration to
370 evaluate the predictions in a χ test. This parameter k has been set equal to 5. Instead in RF,
371 three parameters have been tuned: (i) the maximum depth of the tree (set to 10), (ii) the number
372 of trees in the forest (set to 20), (iii) the minimum number of samples required to split an
373 internal node (set to 40).

374 The two algorithms have been used to estimate the extension of debris and they have been
375 compared using the R-squared and the mean absolute relative distance (MARD).

376 The R-squared measure provides a measure of how well future samples are likely to be
377 predicted by the model by evaluating how much the scatter points are distant from the
378 regression fit line calculated by the algorithm. R-squared measure ranges from 0 to 1, where 1
379 means perfect matching. MARD is the average vertical distance between each point and the
380 regression line. Therefore, the lower the value of MARD and the more accurate the predictions.

381 Results from the training of the algorithms show that KNR algorithm gives a better MARD
382 score (0.32), but a lower value of R-squared (0.42) with respect to RF, which means that more
383 data are needed for KNR. Instead, RF gives better results both in terms of R-squared (0.52)
384 and MARD (0.22) and therefore this algorithm has been selected and implemented in the
385 platform.

386

387

5. POWER GRID

388 Urban PGs consist of a transmission system, which runs for long distances at high voltages,
389 and a distribution system, which delivers electricity at medium and low voltage. The low

390 voltage line (i.e. 230 V single-phase, 400 V three-phase for European countries) supplies
391 domestic and small commercial customers. Usually, at the city-level, PGs follow the main
392 streets and may run both overhead and underground.

393 Various methodologies are available in the literature to assess the seismic damage to the
394 electric infrastructure (Cavalieri, Franchin, Buriticá Cortés, et al., 2014). However, they require
395 a large amount of data about the network's components, which is often not shared by
396 stakeholders and public authorities.

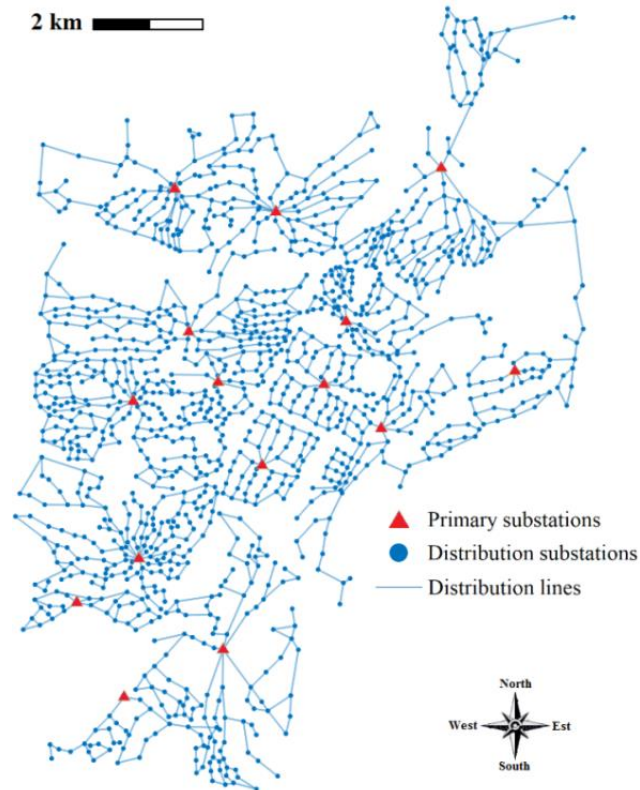
397 Moreover, most of these methods assess the resilience of power distribution networks
398 adopting the inherent fragility of the electrical components. However, in most cases, electrical
399 components can withstand seismic excitation, while the buildings where they are installed are
400 subject to serious seismic damages. The debris generated from partial or complete collapses
401 damages electrical components, compromising the functionality of the entire PG. The weakest
402 element of PGs are often distribution substations as discussed in Fujisaki et al. (2014). Fragility
403 of substations varies whether their components are anchored or unanchored. Cavalieri,
404 Franchin, and Pinto (2014) reported a complete overview of the main recent works on fragility
405 functions of electric power system components, with the indication of the methodology used
406 to evaluate the curves, the components considered and the damage states and indices.
407 Considering the HAZUS methodology (Agency, 2003), to have extensive level of damage (i.e.,
408 repairs needed to restore functionality), the median peak ground acceleration (PGA) should
409 reach 0.34g for low voltage substations with unanchored components and 0.45g in case of
410 anchored components. These values of PGAs are most likely to cause serious building damage
411 given the typical built environment of European cities. Therefore, in this paper, the

412 vulnerability of the PG is related to the damage occurring to the buildings where substations
413 are located. In other words, if the building where a substation is installed collapses, the grid
414 components in that substation fail. Consequently, when a substation fails the electric load drops
415 to zero, and all the buildings connected to that substation are without power.

416 The fragility of distribution lines has not been considered since at the urban level distribution
417 lines are more robust than distribution substations. Distribution lines can run both overhead
418 and underground, despite modern cities prefer to let the system run underground as it is safer
419 and more efficient. In Ideal City, they are mainly meant to be underground. Generally, failure
420 of underground lines happens only in case of strong shakes with significantly large ground
421 deformations, which would cause serious building damage anyway. On the other hand,
422 overhead distribution lines are mostly affected by strong winds, while their vulnerability to
423 earthquakes is limited due to the small size and slenderness of urban utility poles.

424 Ideal City's PG consists of 15 primary substations and 1274 distribution substations (Figure
425 7). The primary substations operate at high and medium voltages and are supposed to be

426 located in robust facilities so that they can keep operating even after strong ground motions.



427

428

Figure 7. *Ideal City's* PG.

429

430 **5.1 Interdependency between buildings and PG**

431 The power system of *Ideal City* has been modeled following the *Density Design Method*
432 (DDM) proposed by Cardoni et al. (2019). The DDM is based on the idea that the fragility of
433 electric substations is the same as the buildings hosting them. Therefore, the electric
434 components and the buildings where they are located are assumed as a series system with their
435 corresponding fragility functions, so the weakest component limits the overall system
436 reliability. This approach allows to implicitly take into account the interdependency between
437 the power network and the building portfolio. The DDM allows for a detailed analysis of the

438 system, as the PG is specifically designed instead of using an existing database. Thus,
 439 population density, power load density, and system properties (e.g., feeders' length, load types,
 440 buses' redundancy, etc.) are the main design parameters. The first step consists in dividing the
 441 area covered by *Ideal City* into districts to locate primary substations. These are characterized
 442 by a medium voltage (MV) scheme of 22 kV. Then, electrical loads are identified following
 443 the procedure described by the 2016 European guidelines (Prettico et al., 2016). Based on the
 444 area and population of each district, the design load is estimated. In detail, the adopted design
 445 load density is assumed to be 8 MVA/km² for each district. This information is needed to
 446 identify the distribution substations containing transformers. Transformers can be of three
 447 types, i.e., 0.40 MVA, 0.63 MVA, and 1.00 MVA. The chosen distribution is 60%, 30%, and
 448 10% respectively, in accordance with current best practices. Overall, *Ideal City*'s PG consists
 449 of 1,274 distribution substations. Table 2 summarizes the number of distribution substations
 450 for each power category.

451 Table 2. *Ideal City*'s distribution substations.

Distribution substation type	Total number
0.40 MVA	766
0.63 MVA	382
1.00 MVA	126

452
 453 Distribution substations are evenly located in the district considering power demand so that
 454 each of them supplies a different number of buildings. Substations located in buildings that are
 455 extensively damaged or collapsed after an earthquake are assumed to fail. Besides, since the
 456 distribution substations are connected in series, once a substation fails all the downstream

457 substations will also be unfunctional. Consequently, the number of buildings and users not
458 supplied after the seismic event can be determined.

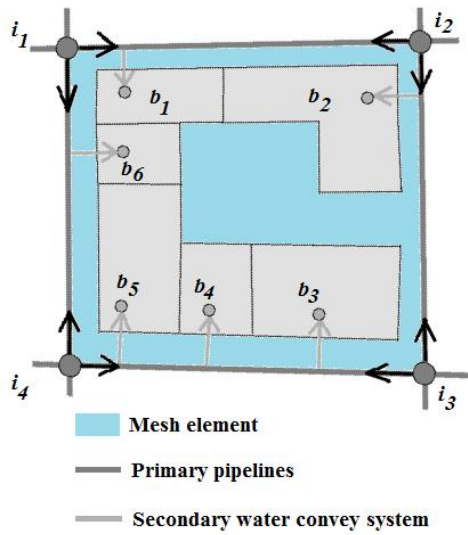
459 **6. WATER DISTRIBUTION NETWORK (WDN)**

460 The WDN serviceability implies enough water supply to fulfill the demand and reasonable
461 water pressure. The damages induced by seismic events are likely to cause a drop in the water
462 pressure and consequently a limited water supply.

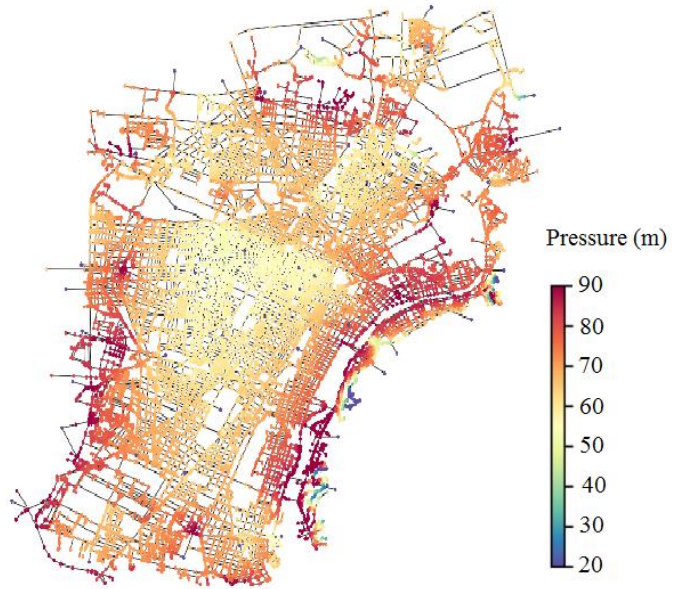
463 In this research, urban water consumption is extrapolated from national census data and the
464 layout of the WDN of *Ideal City* has been assumed to overlap the RTN. Elevations of WDN's
465 nodes have been gathered from Google Maps (Svennerberg, 2010). Collected data have been
466 processed through the Water Network Tool for Resilience, which is a Python package designed
467 to simulate and analyze the resilience of water distribution networks. This tool allows
468 controlling EPANET 2.0 (Rossman, 2000) using Python.

469 The water demand at each node (junction) depends on the number of people served by that
470 node. The number of the population served by each node has been estimated from the number
471 of households around that node.

472 Water distribution systems consist of interconnected components including primary and
473 secondary pipelines, storage facilities, and components that convey water on buildings based
474 on the closest distance between the primary pipeline and the buildings inside the mesh (Figure
475 8a).



(a)



(b)

476

477 **Figure 8.** (a) Water demand in w^{th} element, i^{th} nodes of the element, and water convey on

478 buildings within the element. (b) Water pressure of the WDN after calibration.

479

480 The calibration of a WDN of such a size brings on several difficulties. It is a fundamental

481 issue to ensure an accurate and realistic simulation for both the flow velocity and pressure. The

482 pipes diameters and the positions of the valves, pumps, reservoirs, and tanks have been

483 determined to ensure the following constraints (Equations (4),(5)):

$$484 \quad 0.5m / s \leq \text{Velocity} \leq 2m / s \quad (4)$$

$$485 \quad 40m \leq \text{Pressure} \leq 80m \quad (5)$$

486 Figure 8b shows the calibrated WDN at the peak hour of water demand. More details about

487 the network's generation methods and technical criteria can be found in (Taurino et al., 2018).

488

489 **6.1 Vulnerability of the WDN**

490 The reliability of a water network is connected to the concept of vulnerability of its elements.
491 Herein, the focus is given to the pipe because it is the most challenging component to inspect
492 and replace, and also its extensive distribution and exposure make it especially vulnerable. In
493 this work, the seismic vulnerability of the buried pipelines introduced in the American Lifelines
494 Alliance (Eidinger et al., 2001) is adopted.

495 The seismic wave propagation induces strains to the pipes due to the soil-pipe interaction.
496 Strains could produce damage if the pipe strength is exceeded. When pipe damage occurs, the
497 pipe is assumed to break in the middle. In the context of this work, only major damage is
498 assumed to cause water leakage. Pipe damage is modeled dividing the pipe into two equal parts.
499 Then two reservoirs are added at their endpoints to simulate the water leakage through the
500 crack. The reservoirs have a total head equal to the elevation of the middle point of the pipe
501 (assuming that the pipe breaks in the middle). A check valve is inserted so that water only flows
502 towards the reservoirs.

503 A combined demand-driven and pressure-driven analysis is conducted to account for the
504 dependence of water supply on pressure. First, a Demand-driven analysis is performed; then,
505 nodes with pressure below the value required to satisfy the demand are converted into Emitter
506 nodes.

507 **6.2 Interdependency between buildings and WDN**

508 Once a seismic event occurs, an additional drop of pressures might be considered due to the
509 damage to the secondary water system. In this study, a further drop of pressure in the pipelines
510 system is considered when “extensive” or “complete” damage occurs in a household located

511 within the closed-shaped WDN. In other words, the building damage scenario is used to update
512 the water supply of the WDN.

513 **6.3 Interdependency between PG and WDN**

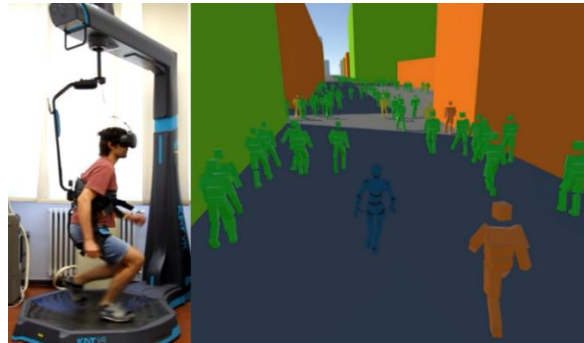
514 The functionality of WDN is dependent on the power system due to the presence of pumps
515 and electric valves. In the aftermath of a seismic event, a power outage may occur leading to a
516 temporary inoperability of the electric device of the WDN. In this study, the interdependency
517 between PG and WDN is taken into account by identifying the unpowered pumps and then
518 updating the EPANET model accordingly. A new state of nodal pressure and water supply is
519 then generated.

520 **7. EMERGENCY EVACUATION MODELLING**

521 The implemented platform includes STN that consist of an agent-based model (ABM), which
522 can manage 900,000 individual agents that dynamically interact with each other and with the
523 urban scenario. Furthermore, the ABM can be used to model other objects, such as shelters,
524 hospitals, and ambulances that are governed by different rules. Therefore, an emergency
525 evacuation can be simulated, and specific emergency plans can be designed to study and
526 improve the community response.

527 The ABM layer is also able to manage the interdependency between the agents and the other
528 layers (i.e. the built environment, the generated debris, and the road network). Furthermore, the
529 evacuees have been implemented with individual characteristics including human behavior and
530 considering different levels of agent health obtained from the seismic damage simulation.
531 Figure 9 reports evacuating agents, where the level of injury severity is associated with the

532 agent color (e.g. green normal conditions, orange slight injured), and the evacuation velocity
533 depends on the injury level.



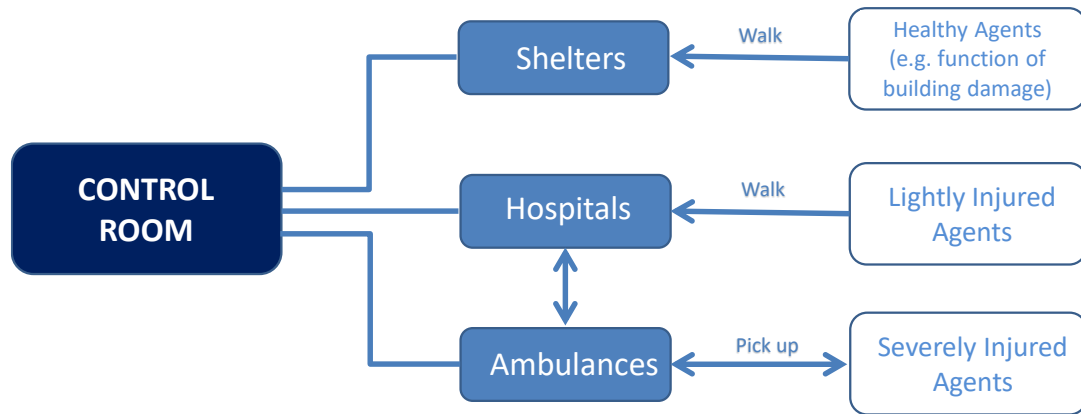
534

535 **Figure 9.** Simulation of an evacuation procedure using virtual reality. The color of each
536 agent indicates her health conditions.

537 The ABM environment has been developed in Unity (UnityTechnologies, 2020). The input
538 data needed to develop the ABM scenario are collected from the other infrastructure layers
539 implemented in the platform. Indeed, the data collected are: (i) the estimated post-disaster
540 building damage that reflects in (ii) number of injuries and (iii) road blockage due to debris.

541 **7.1 First aid modeling**

542 The ABM STN layer considers two classes of agents, the individuals, and the ambulances;
543 the last ones pick up severely injured individuals and transport them to hospitals. On the
544 contrary, lightly injured agents preserve their walking capabilities and reach hospitals on their
545 own (Figure 10). Healthy agents can remain close to their buildings or walk to the nearest
546 emergency shelter accordingly to a random procedure that is parameterized as a function of
547 damage level suffered by the buildings.



548

549

Figure 10. First-aid organization in the ABM layer.

550 Shelters have a fixed capacity, beyond which the individual starts walking toward the closest

551 town exit. Also, hospitals have a fixed capacity, except for those that can deploy a field hospital.

552 In this case, an infinite capacity is assumed to guarantee assistance to all injured individuals.

553 A control room manages the hospitals and shelters monitoring the available information and

554 making decisions about resources. The buildings may contain a number of individuals and

555 contain a variable number of individuals function of the time of the day.

556 7.2 Modeling human behavior and emotions in ABM

557 During the emergency evacuation, two frequent individual phenomena can be recognized:

558 the leader-follower and the emotional (e.g. altruism, panic) behavior. The first one is

559 recognized as the static and predictable component because it remains unchanged throughout

560 the process. Instead, the second one, the dynamic component, is generally unpredictable

561 because characterized by emotions. It can be modeled using the Belief-Desire-Intention (BDI)

562 model and implemented through a matrix approach by the Extended Decision Field Theory

563 (EDFT) to cope with the dynamically changing environment (G. P. Cimellaro et al. (2019), G.

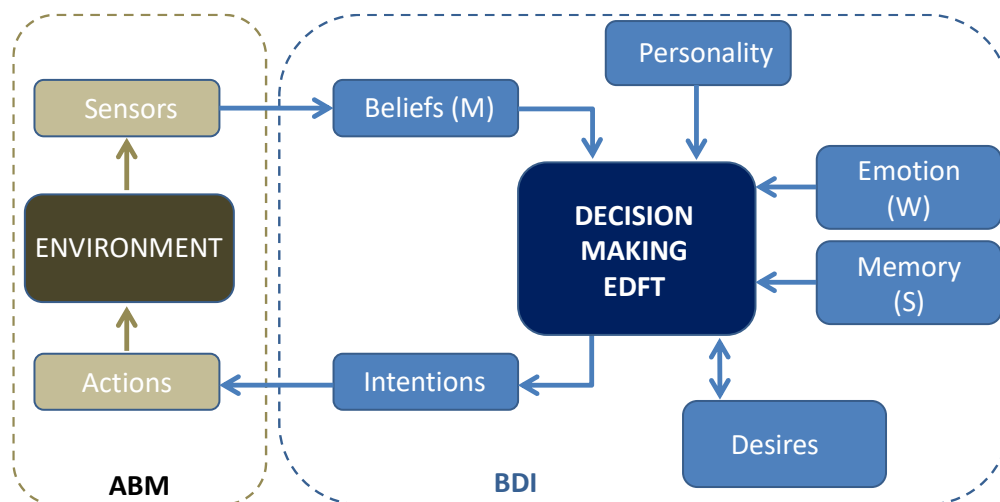
564 P. Cimellaro et al. (2017)). It presents a dynamic and probabilistic mathematical approach to

565 reproduce the individual decision-making process in the changing environment. It is
 566 summarized by the following relation that allows to compute the preferences P among m
 567 options expressed by an agent during the simulation time (Equation (6)).

$$568 \quad P(t+h) = SP(t) + CM(t+h) \cdot W(t+h) \quad (6)$$

569 where $P(t)^T = [P_1(t), P_2(t), \dots, P_m(t)]$ are the preference in percentage and $P_i(t)$ is the strength
 570 of the preference corresponding to option i at time t . The first term is the product of the
 571 preference chosen at the previous state and the stability matrix S that provides the memory
 572 effect. The second term reproduces the emotional individual behavior in the changing
 573 environment, where M is the value matrix that represents the subjective evaluations
 574 (perceptions) of a decision-maker, W is the weight vector that allocates the weights of attention
 575 corresponding to each attribute of M , and C is the contrast matrix that compares the weighted
 576 evaluations of each option. Matrix C is the identity matrix if each option is evaluated
 577 independently (G. P. Cimellaro et al. (2019), G. P. Cimellaro et al. (2017)).

578



579

580 **Figure 11.** EDFT architecture and interaction of the human behavior modules (adapted

581 from G. P. Cimellaro et al. (2019).

582

583 **7.3 Interdependencies with other networks**

584 The interdependency between the evacuees and the built environment consists of the debris
585 generated by the earthquake-induced damages to buildings. As a cascading consequence of
586 debris accumulation, the road network can be interrupted entailing an overall increase in the
587 average number of people who have difficulty evacuating and an essential risk that some
588 individuals cannot evacuate at all. Furthermore, the first aid network supported by ambulances
589 that intervene in the recovery of seriously injured individuals can be unable to access those
590 parts of the urban system most affected by damage to buildings and debris.

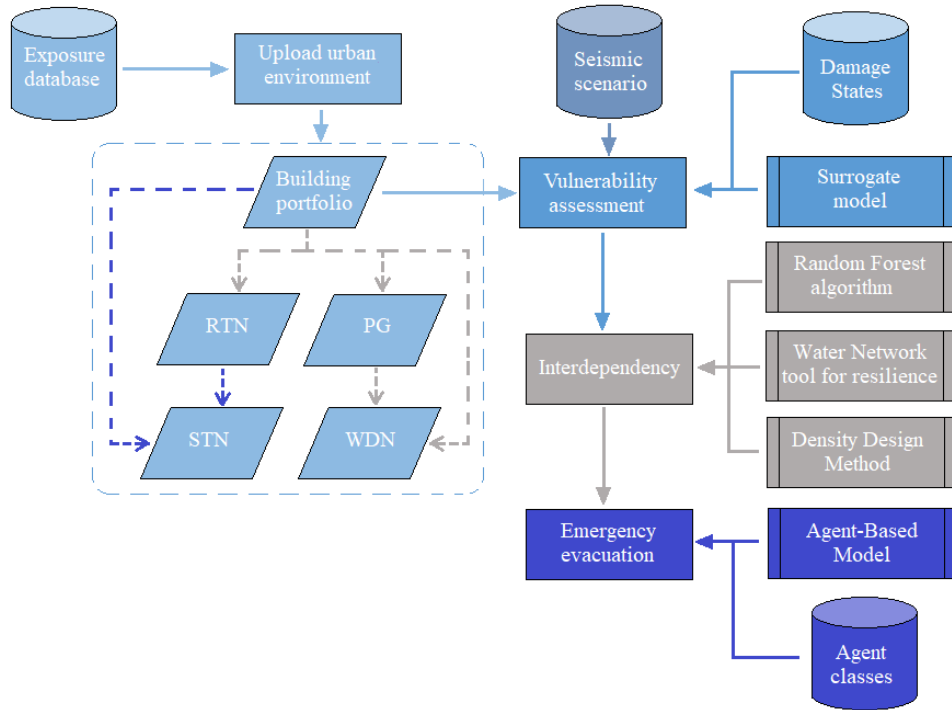
591 The debris generation is also included in the ABM layer with the approach already detailed
592 in Section 4.1. Thus, the hybrid characteristics of *Ideal City* allow both the estimation of
593 buildings' damage and debris' generation and the analysis of their cascading effects. In detail,
594 individuals could be killed, injured, or trapped inside damaged buildings or *Ideal City* portions.
595 Moreover, the transportation network can be interrupted blocking the ambulances' intervention
596 and affecting the escape routes for evacuees.

597

597 **8. APPLICATION**

598 The objective of this work is the development of an integrated platform to assess seismic
599 resilience at the community level for large-scale areas. Five layers have been considered to
600 model community infrastructures, while different physical methods have been implemented to
601 evaluate the infrastructures' vulnerability and their mutual interdependencies. The flowchart

602 depicted in Figure 12 provides a detailed description of the methods and processes used in the
 603 platform.



604

605

Figure 12. Flowchart of the integrated platform.

606

607

608

609

610

611

612

613

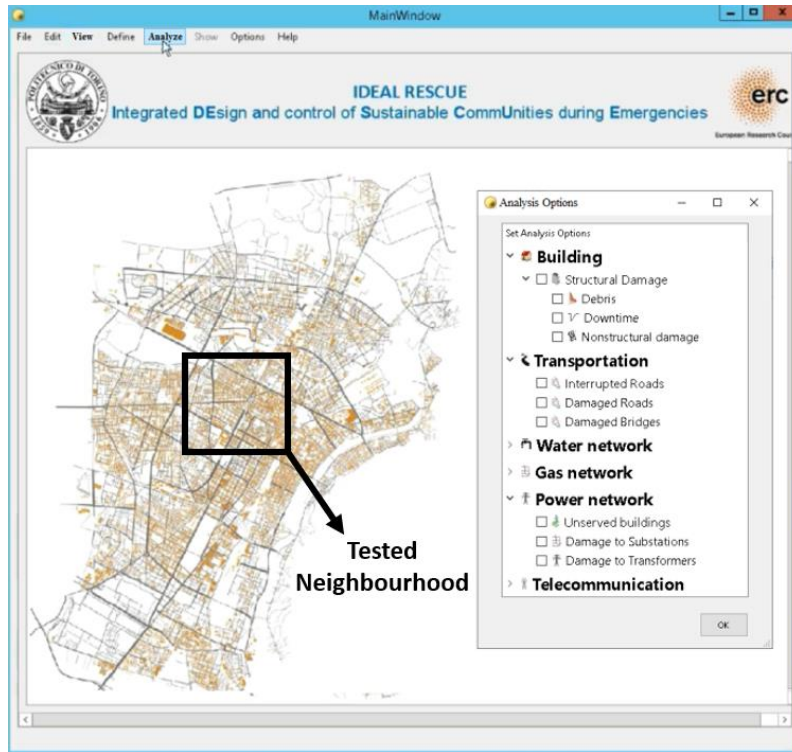
614

All the inherent data of the infrastructures are stored in the exposure database. Building stock represents the main physical layer whose vulnerability is assessed by using a *surrogate* model based on certain damage states and seismic scenario. The platform allows users to upload exposure database, while selecting the damage states and the related Engineering Demand Parameters. Ghobarah (2004) damage states and related maximum inter-story drift thresholds are set by default in the integrated platform. The user can also define the seismic scenario by selecting (i) epicenter location, (ii) magnitude of the earthquake, (iii) time-history recorded at the epicenter, and (iv) ground motion prediction equation to evaluate the geometrical attenuation at any building location. Ambraseys et al. (1996) attenuation model is set by default

615 while seismic record processing is performed by the embedded OpenSignal tool (Cimellaro &
616 Marasco, 2015).

617 The simulated damage experienced by the buildings is the starting point for taking into
618 account the cascading effects on the RTN, PG, and WDN. Interdependency between buildings
619 and roads is accounted through an RF algorithm which provides the functionality state of each
620 roadway element. Furthermore, the Density Design Method is applied to PG by setting off the
621 transformers located within irreversibly damaged buildings. Based on the buildings' damage
622 and PG's unfunctionality, the Water Network tool for resilience is employed to evaluate the
623 effects on the WDN. Under these conditions, the emergency evacuation is simulated through
624 an Agent-Based model after fixing the common rules adopted by the agents.

625 An application of the developed platform to *Ideal City* hybrid model is herein presented. The
626 virtual city consists of 23420 residential buildings and covers an overall area of 120 km² with
627 a population of 908.129 inhabitants. The building stock of the city is mainly composed of RC
628 buildings (63%) and masonry structures for the remaining parts (37%). Figure 13 illustrates a
629 screenshot of the software's graphical user interface and the related analysis options.



630

631 **Figure 13.** View of *Ideal City* within the software’s main window and the dataflow for a
 632 disaster simulation.

633 Different seismic scenarios have been adopted by defining the epicenter location, the moment
 634 magnitude, and the time history recorded at the epicenter. Geometrical attenuation at any
 635 building location has been estimated based on Ambrases’ attenuation Ground Motion
 636 Prediction Equation (GMPE) (Ambraseys et al., 1996).

637 Four benchmark horizontal acceleration time histories have been selected using Opensignal
 638 software (Cimellaro & Marasco, 2015). Northridge (Imar County Hospital parking lot in
 639 Sylmar, California) and Kobe (Kobe Japanese Meteorological Agency station, Japan) records
 640 have been assumed to simulate the effects of near-field earthquakes. On the other hand, El
 641 Centro (Imperial Valley Irrigation District substation, California) and Hachinohe (Hachinohe

642 City, Japan) records have been considered as far-field seismic benchmark scenarios. Table 3
 643 lists the main seismological characteristics of each selected record.

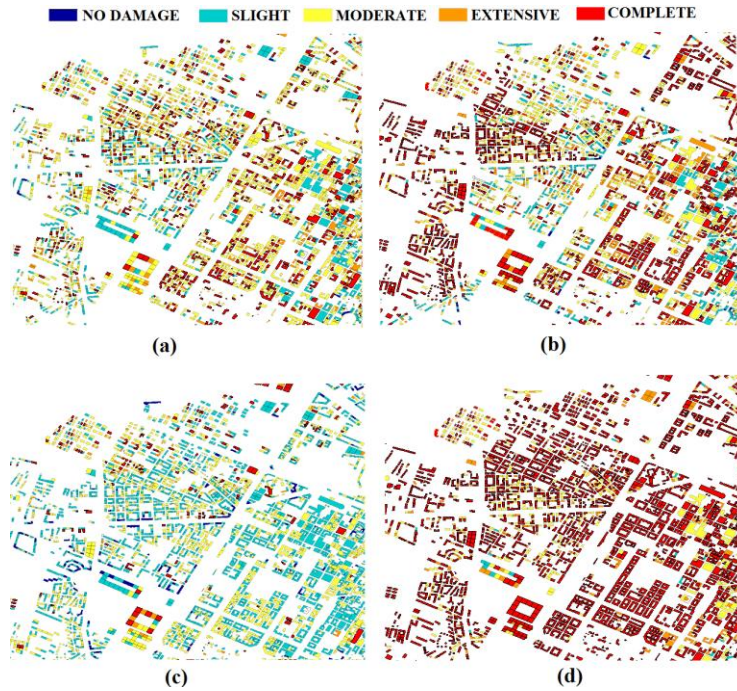
644 Table 3. Characteristics of the four selected benchmark time histories.

	El Centro	Kobe	Hachinohe	Northridge
Date	5/18/1940	1/17/1995	5/16/1968	1/17/1994
Event	Imperial Valley	Hyogoken Nanbu	Tokachi-oki	California
M _w	6.9	6.8	8.2	6.7
Depth [km]	16.00	17.60	26.00	11.30
PGA [g]	0.35	0.82	0.23	0.84

645
 646 The developed platform can provide damage information associated with all the layers of the
 647 analyzed area. Furthermore, the dataflow can be completely managed by the user who can
 648 choose among different options (Figure 13). Analysis flow starts with the damage assessment
 649 on the building portfolio. Once a seismic scenario is defined, a pair of horizontal orthogonal
 650 acceleration time histories have been applied at each building location by considering the
 651 geometrical attenuation.

652 Figure 14 depicts the Damage States (DSs) map of the selected district under different
 653 seismic scenarios. Table 4 lists the percentage of building DSs: Northridge and Kobe scenarios
 654 mainly have caused almost complete damage (about 86% and 79% of buildings, respectively).
 655 Only a few buildings have been found functional (around 1% ranging between undamaged and
 656 slightly damaged for both scenarios). Besides, 40% of moderate damage and 27% of complete
 657 damage has been experienced by the El Centro earthquake, while extensive and slight damage

658 corresponds to 14% and 19%, respectively. Hachinohe earthquake is the less disruptive
 659 scenario where most of the buildings remain functional, 52% of buildings are either undamaged
 660 or slightly damaged, 37% are moderately damaged, while only 9% collapse.



661
 662 **Figure 14.** Building DS maps of *Ideal City* district for (a) El Centro, (b) Kobe, (c)
 663 Hachinohe, and (d) Northridge earthquake scenarios.

664 Table 4. Percentage of buildings DSs for each scenario.

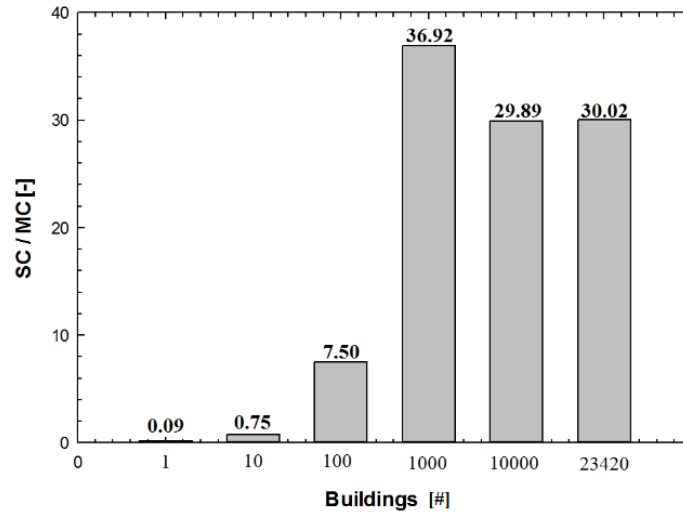
Damage States [%]	El Centro	Kobe	Hachinohe	Northridge
No damage	0.62	0.03	5.9	0.03
Slight	18.75	0.77	45.68	0.77
Moderate	39.38	9.53	36.73	7.17
Extensive	14.1	10.21	2.22	5.83

Complete	27.14	79.47	9.47	86.19
----------	-------	-------	------	-------

665

666 The possibility to use parallel computing to run this demanding computational analysis has
667 been investigated. First, Single Core (SC) and Multi-Core (MC) processing have been
668 compared in terms of elapsed time under different building cluster sizes. Figure 15 illustrates
669 the variability of the mean elapsed time ratio (speedup ratio) vs the number of buildings
670 involved during the analysis.

671 According to the numerical results, SC application is faster when the number of buildings is
672 lower than 10. This is because MC frameworks require more time for spawning processes,
673 assigning tasks, collecting data, and closing processes. Once the processes are spawned, they
674 can be used without closing processes. In the selected case study, the speedup ratio of MC
675 reaches the maximum efficiency when 1000 buildings are analyzed simultaneously. Under this
676 condition, MC is 36 times faster than SC. When the top performance is reached, then an
677 increase of the elapsed time is observed due to the thermal throttling caused by the CPU
678 overheating. Under this condition, the new speedup ratio is about 30 times faster than SC and
679 remains almost constant until the end of the analysis.



680

681

Figure 15. Speedup ratio between Single-Core (SC) and Multiprocessing (MC)

682

computational process.

683

684

685

686

687

688

689

Once the building damage has been estimated, then different types of interdependencies have been investigated. First, the extension of debris caused by the building damage is evaluated using a machine learning algorithm and the corresponding obstructed roads are identified. Figure 16 illustrates the interrupted roads (red lines) caused by the four selected seismic scenarios for the considered district. Indeed, the Northridge earthquake has caused the largest number of blocked roads (30.48%) followed by Kobe (21.29%) and El Centro (14.49%), while Hachinohe is the less disruptive seismic event with only 4.47% of unfunctional roads.

690

691

692

693

694

695

The blocked roads are not equally distributed over the city. Indeed, some districts are completely isolated due to the amount of debris produced, highlighting the importance of this type of analysis to plan efficient evacuation and rescue operations. The *average vertex degree* and *global efficiency* have been calculated and normalized with respect to the undamaged conditions. Results are shown in Figure 17 where it is possible to see the two indices reducing with the increment of the earthquake severity.

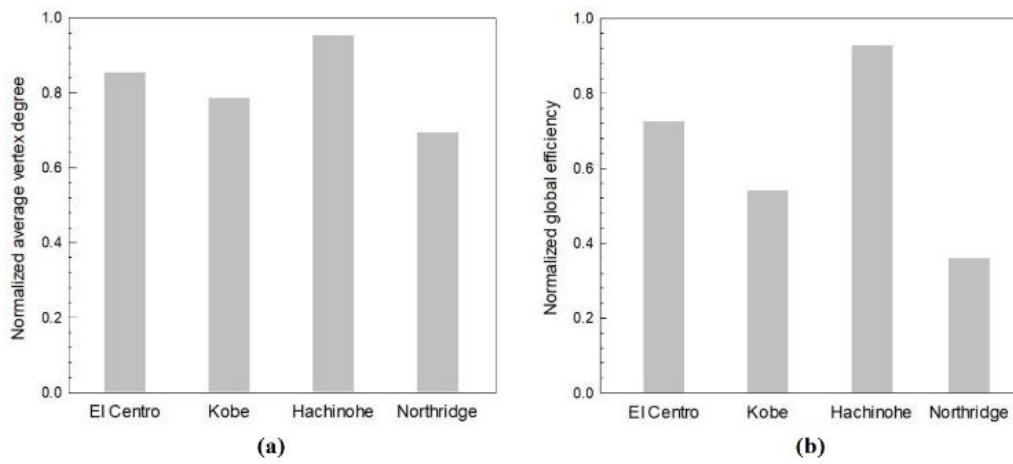


696

697

698

Figure 16. Visualization of interrupted roads for (a) El Centro, (b) Kobe, (c) Hachinohe, and (d) Northridge earthquake scenarios.



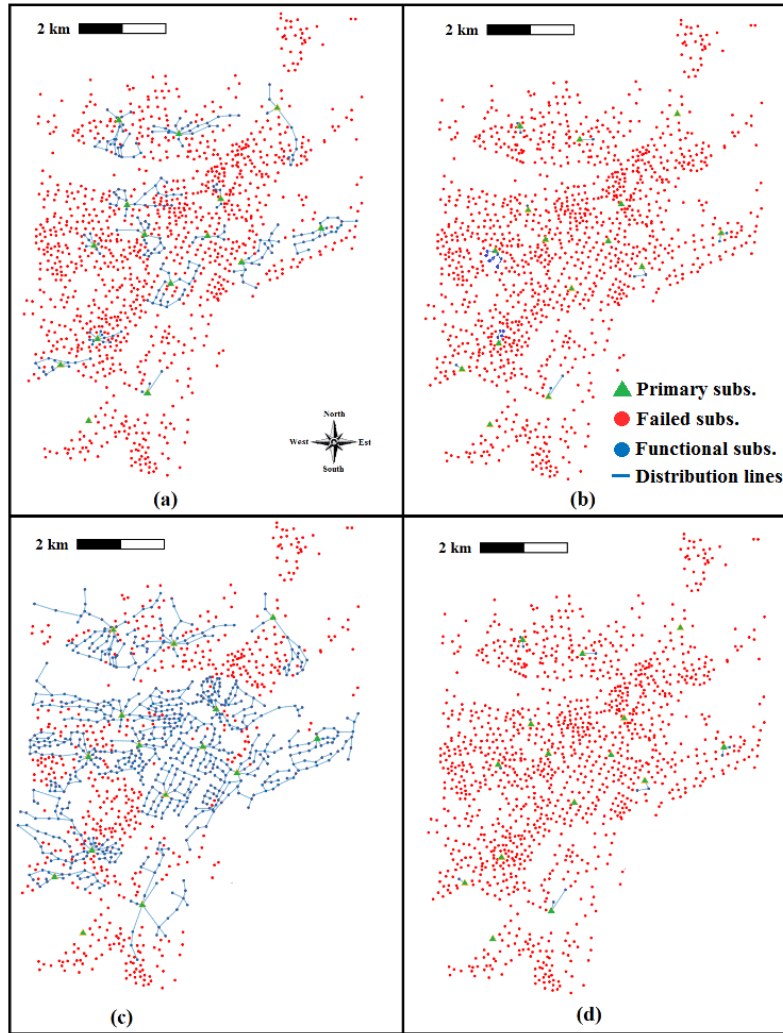
699

700

701

Figure 17. Variation of the normalized average vertex degree (a) and normalized global efficiency (b) under different seismic scenarios.

702 The second interdependency that has been considered correlates the power distribution
703 network with the building damage. The failed electrical substations for the four different
704 seismic events are shown in Figure 18.

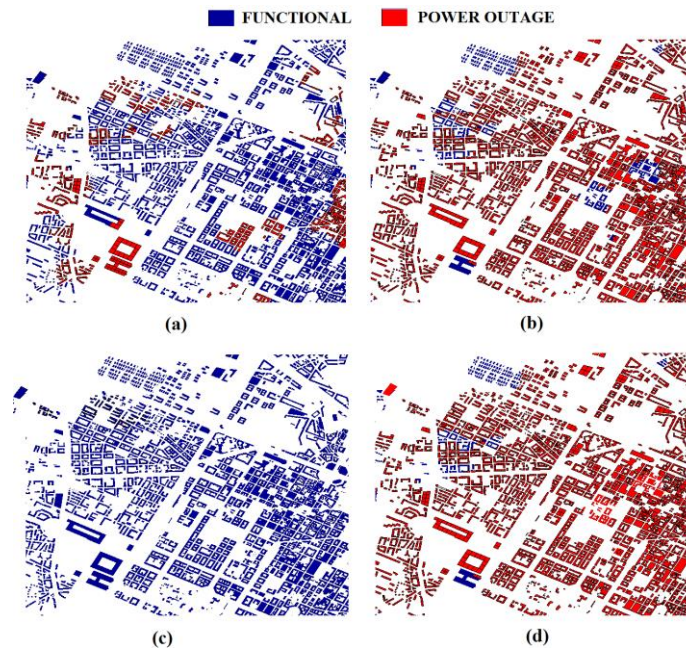


705
706 **Figure 18.** Visualization of PG failure's component for (a) El Centro, (b) Kobe, (c)
707 Hachinohe, and (d) Northridge earthquake scenarios.

708 In detail, the substations that remain functional for Northridge are 12, for Kobe are 25, while
709 for El Centro are 220, and for Hachinohe are 747 out of a total of 1274 substations. These
710 results show that the near-field earthquakes are more disruptive than the far-field earthquakes

711 for the PG. In Figure 19 is shown the impact of the PG's disruption at the building level, where
712 in red are the buildings without power.

713 A simple resilience index (R_{power}) has been introduced as the ratio between the number of
714 users who still have access to electricity and the total population of *Ideal City*. 98.5% of the
715 population is without power after Northridge and Kobe scenarios, while about 80% of the
716 population has no power after the El Centro earthquake. Instead, Hachinohe causes a loss of
717 power for about 40% of users.



718

719 **Figure 19.** Visualization of buildings with and without electricity for (a) El Centro, (b)

720

Kobe, (c) Hachinohe, and (d) Northridge earthquake scenarios.

721

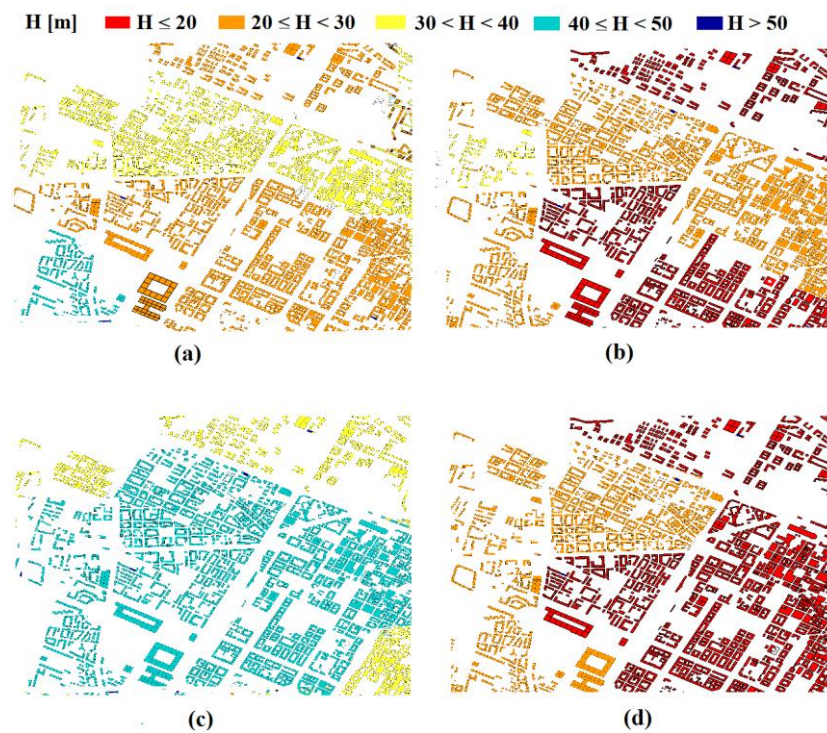
722

Finally, the damage caused by the four benchmark scenarios on the WDN has been investigated. Northridge scenario induced the highest number of damaged pipes while

723

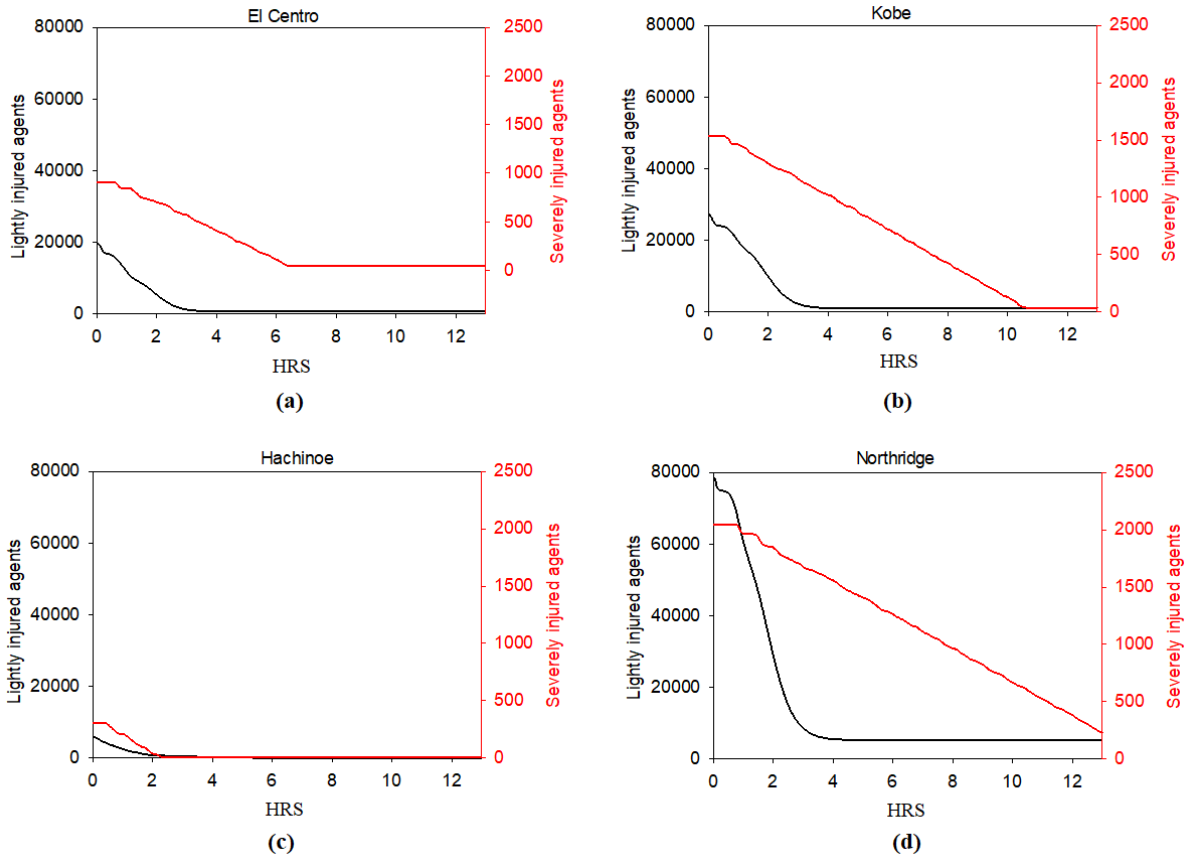
Hachinohe induced the lowest one.

724 Figure 20 depicts the drop in water pressure (m) in each building caused by the damage on
725 the water pipes. The Northridge scenario induced the highest number of damaged pipes while
726 Hachinohe induced the lowest one. The disruption of the pipes is a function of the earthquake
727 characteristics, such as Magnitude, epicenter, depth, etc. Looking at Table 3 in the paper,
728 Northridge earthquake, due to its shallow depth, is a near field earthquake. This makes it more
729 disruptive for the water pipes of the *Ideal city*.



730
731 **Figure 20.** Water pressure distribution after (a) El Centro, (b) Kobe, (c) Hachinohe, and (d)
732 Northridge earthquake scenarios.

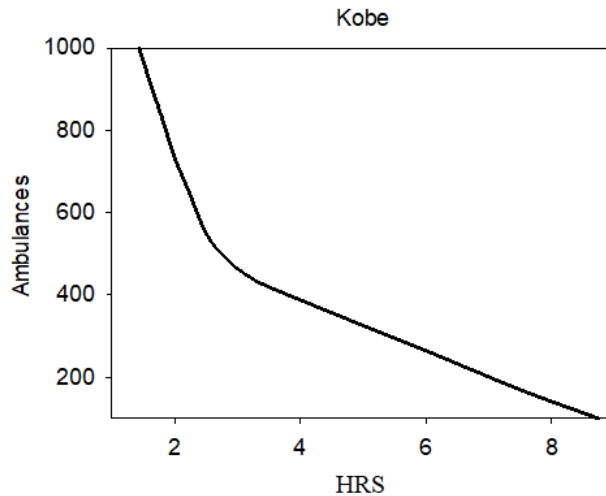
733 Finally, the population response to emergency evacuation has been analyzed by the ABM
734 layer of *Ideal City*. For example, the number of lightly injured individuals walking to hospitals
735 and severely injured individuals that are waiting to be rescued are reported in Figure 21.



736

737 **Figure 21.** Lightly injured agents walking to hospitals and severely injured waiting to be
 738 rescued vs time (hours): (a) El Centro, (b) Kobe, (c) Hachinohe, and (d) Northridge
 739 earthquake scenarios.

740 Furthermore, the platform can also be adopted at the design stage, e.g. to compute the
 741 minimum number of rescue resources (ambulances) to recover the seriously injured
 742 individuals within a fixed period for a certain earthquake scenario (Figure 22).



743

744 **Figure 22.** Kobe event: rescue time (hour of all severely injured individuals as a function
 745 of the number of ambulances.

746 The four seismic benchmark scenarios have caused similar effects for all the infrastructures
 747 within *Ideal city*. Northridge and Kobe have found to be more disruptive due to the higher
 748 PGA. These two near-field seismic scenarios have caused more than 90% of irreversible
 749 damage to the building portfolio. Their impact on the RTN have been also devastating, causing
 750 a considerable decrease in the normalized global efficiency of the transportation network
 751 around 45-55%. A similar trend has been found in the PG, where more than 98% is without
 752 power following the Northridge and Kobe earthquakes. Drastically reduction of water pressure
 753 has been also accounted for in the WDN after the occurrence of the two aforementioned
 754 seismic scenarios. Finally, the number of severely injured agents between 50000 and 60000
 755 has been estimated.

756 The Hachinoe scenario has found as the less disruptive scenario for all the networks, while
 757 El Centro induced a considerable level of irreversible damage on the analyzed infrastructure.
 758 More than 40 % of building stock has experienced irreversible damage following the El Centro

759 scenario, while only 12 % has been found for Hachinoe. These results are also reflected on the
760 RTN, where 75% and 40% of normalized global efficiency have been accounted. 20% and
761 60% of substations have been found functional following El Centro and Hachinoe scenarios,
762 respectively. Finally, Hachinoe has caused only 10000 severely injured agents, while after the
763 occurrence of El Centro scenario, more than 35000 severely injured agents have been found.

764 The large outcomes discrepancies between Hachinoe and El Centro are due to their
765 seismological characteristics. Hachinoe is represented by a greater magnitude and hypocentral
766 depth than El Centro. Therefore, the seismic wave propagation associated with the Hachinoe
767 scenario is more affected by the geometrical attenuation. In fact, the PGA of Hachinoe is about
768 0.23g, while 0.35g is the one of El Centro. In the nonlinear time history analyses, such a kind
769 of discrepancy of PGA will cause considerably different responses.

770 **9. CONCLUDING REMARKS**

771 A computational platform is presented in this paper to analyze the effects of seismic events
772 on an urban community. The platform implements different layers, such as buildings, road
773 transportation networks, power grid, water distribution networks, and socio-technical
774 networks. Specific models have been developed to simulate the interdependency between
775 different layers. The individual seismic response of each building is analyzed through a
776 *surrogate* physical model, including inherent uncertainties. The seismic effects in terms of
777 damage and serviceability for each layer can be computed and visualized. Furthermore, an
778 agent-based model has been developed to simulate the emergency evacuation process and the
779 first-aid operations in post-disaster conditions. Future work is geared towards including gas
780 and telecommunication interdependencies in the analyses.

781 A hybrid model of a virtual city has been used to test the platform under four different seismic
782 scenarios. The main innovative aspects and advantages of the proposed platform are: (i)
783 damage and resilience assessment of critical infrastructures in a large-scale urban environment
784 considering their interdependencies; (ii) graphic visualization of the results obtained by the
785 different layers; (iii) multiprocessing computation; (iv) agent-based modeling for emergency
786 management and evacuation.

787 The platform is intended to support decision-makers and planners to analyze the community
788 response to a seismic event and implement possible countermeasures to improve the overall
789 resilience. The long-term objective is to make individual infrastructures safer, implementing
790 specific actions that allow each network to withstand external perturbations and to mitigate
791 cascading effects due to interdependencies.

792 The current state of the platform does not allow considering the recovery of the damaged
793 structure and infrastructure. This is actually a work in progress that will be included in a future
794 paper. The future work will address both the damage and the restoration analysis of the
795 infrastructure network by incorporation already-developed models within the platform (De
796 Iuliis et al., 2019; Kammouh, Cimellaro, et al., 2018).

797

798

ACKNOWLEDGMENTS

799 The research leading to these results has received funding from the European Research
800 Council under the Grant Agreement n° ERC_IDEal reSCUE_637842 of the project IDEAL
801 RESCUE— Integrated DEsign and control of Sustainable CommUnities during Emergencies.

802

REFERENCES

803 Agency, F. E. M. (2003). Hazus MR4 Multi-Hazard Loss Estimation Methodology.
804 Alsubaie, A., Alutaibi, K., & Martí, J. (2015). *Resilience assessment of interdependent critical infrastructure*.
805 Paper presented at the International Conference on Critical Information Infrastructures Security.
806 Ambraseys, N. N., Simpson, K. u., & Bommer, J. J. (1996). Prediction of horizontal response spectra in Europe.
807 *Earthquake Engineering & Structural Dynamics*, 25(4), 371-400.
808 Ament, M., Knittel, G., Weiskopf, D., & Strasser, W. (2010). *A parallel preconditioned conjugate gradient solver*
809 *for the poisson problem on a multi-gpu platform*. Paper presented at the 2010 18th Euromicro
810 Conference on Parallel, Distributed and Network-based Processing.
811 Balaei, B., Wilkinson, S., Potangaroa, R., & McFarlane, P. (2020). Investigating the technical dimension of water
812 supply resilience to disasters. *Sustainable Cities and Society*, 56, 102077.
813 Bastian, M., Heymann, S., & Jacomy, M. (2009). *Gephi: an open source software for exploring and manipulating*
814 *networks*. Paper presented at the Third international AAAI conference on weblogs and social media.
815 Borgdorff, J., Krishna, H., & Lees, M. H. (2015). Sim-city: An e-science framework for urban assisted decision
816 support. *Procedia Computer Science*, 51, 2327-2336.
817 Cardoni, A., Cimellaro, G., Domaneschi, M., Sordo, S., & Mazza, A. (2019). Modeling the interdependency
818 between buildings and the electrical distribution system for seismic resilience assessment. *International*
819 *Journal of Disaster Risk Reduction*, 101315.
820 Cash, D., Adger, W. N., Berkes, F., Garden, P., Lebel, L., Olsson, P., . . . Young, O. (2006). Scale and cross-
821 scale dynamics: governance and information in a multilevel world. *Ecology and society*, 11(2).
822 Cavaliere, F., Franchin, P., Buriticá Cortés, J. A., & Tesfamariam, S. (2014). Models for seismic vulnerability
823 analysis of power networks: comparative assessment. *Computer-Aided Civil and Infrastructure*
824 *Engineering*, 29(8), 590-607.
825 Cavaliere, F., Franchin, P., & Pinto, P. E. (2014). Fragility functions of electric power stations *SYNER-G:*
826 *typology definition and fragility functions for physical elements at seismic risk* (pp. 157-185): Springer.
827 Cimellaro, & Marasco, S. (2015). A computer-based environment for processing and selection of seismic ground
828 motion records: OPENSIGNAL. *Frontiers in Built Environment*, 1, 17.
829 Cimellaro, Ozzello, F., Vallero, A., Mahin, S., & Shao, B. (2017). Simulating earthquake evacuation using human
830 behavior models. *Earthquake Engineering & Structural Dynamics*, 46(6), 985-1002.
831 doi:10.1002/eqe.2840
832 Cimellaro, Renschler, C., Reinhorn, A. M., & Arendt, L. (2016). PEOPLES: a framework for evaluating
833 resilience. *Journal of Structural Engineering, ASCE*, 142(10), 1-13 DOI: 10.1061/(ASCE)ST.1943-
834 1541X.0001514. doi:[http://dx.doi.org/10.1061/\(ASCE\)ST.1943-1541X.0001514](http://dx.doi.org/10.1061/(ASCE)ST.1943-1541X.0001514)
835 Cimellaro, G. P. (2016). Urban resilience for emergency response and recovery. *Switzerland: Springer [DOI:*
836 *10.1007/978-3-319-30656-8]*.
837 Cimellaro, G. P., Mahin, S., & Domaneschi, M. (2019). Integrating a Human Behavior Model within an Agent-
838 Based Approach for Blasting Evacuation. *Computer-Aided Civil and Infrastructure Engineering*, 34(1),
839 3-20.
840 Cimellaro, G. P., Ozzello, F., Vallero, A., Mahin, S., & Shao, B. (2017). Simulating earthquake evacuation using
841 human behavior models. *Earthquake Engineering & Structural Dynamics*, 46(6), 985-1002.
842 Crowley, H., Pinho, R., Pagani, M., & Keller, N. (2013). Assessing global earthquake risks: the Global
843 Earthquake Model (GEM) initiative *Handbook of seismic risk analysis and management of civil*
844 *infrastructure systems* (pp. 815-838): Elsevier.
845 Cutter, S. L., Barnes, L., Berry, M., Burton, C., Evans, E., Tate, E., & Webb, J. (2008). A place-based model for
846 understanding community resilience to natural disasters. *Global Environmental Change*, 18(4), 598–
847 606.
848 De Iuliis, M., Kammouh, O., Cimellaro, G. P., & Tesfamariam, S. (2019). Downtime estimation of building
849 structures using fuzzy logic. *International Journal of Disaster Risk Reduction*, 34, 196-208.
850 doi:<https://doi.org/10.1016/j.ijdr.2018.11.017>
851 DEEDS. Digital Environment for Enabling Data-Driven Science. Retrieved from <https://datacenterhub.org/>
852 Ding, Y., Zhu, Q., & Lin, H. (2014). An integrated virtual geographic environmental simulation framework: a
853 case study of flood disaster simulation. *Geo-spatial Information Science*, 17(4), 190-200.
854 Domaneschi, M., Cimellaro, G. P., & Scutiero, G. (2019). A simplified method to assess generation of seismic
855 debris for masonry structures. *Engineering Structures*, 186, 306-320.

856 Dudenhoefter, D. D., Permann, M. R., & Manic, M. (2006). *CIMS: A framework for infrastructure*
857 *interdependency modeling and analysis*. Paper presented at the Proceedings of the 38th conference on
858 Winter simulation.

859 EERI. The Earthquake Engineering Research Institute collection of case studies. Retrieved from
860 <http://db.concretcoalition.org/>

861 Eidinger, J., Avila, E., Ballantyne, D., Cheng, L., Der Kiureghian, A., Maison, B., . . . Power, M. (2001). Seismic
862 fragility formulations for water systems. *sponsored by the American Lifelines Alliance, G&E*
863 *Engineering Systems Inc., web site <http://homepage.mac.com/eidinger>.*

864 Fujisaki, E., Takhirov, S., Xie, Q., & Mosalam, K. M. (2014). *Seismic vulnerability of power supply: lessons*
865 *learned from recent earthquakes and future horizons of research*. Paper presented at the Proceedings of
866 9th international conference on structural dynamics (EURODYN 2014). European Association for
867 Structural Dynamics, Porto, Portugal.

868 GEER. Geotechnical Extreme Events Reconnaissance. Retrieved from <http://www.geerassociation.org/>

869 Ghobarah, A. (2004). *On drift limits associated with different damage levels*. Paper presented at the International
870 workshop on performance-based seismic design.

871 Guidotti, R., Chmielewski, H., Unnikrishnan, V., Gardoni, P., McAllister, T., & van de Lindt, J. (2016). Modeling
872 the resilience of critical infrastructure: The role of network dependencies. *Sustainable and resilient*
873 *infrastructure, 1*(3-4), 153-168.

874 Hagberg, A., Swart, P., & S Chult, D. (2008). *Exploring network structure, dynamics, and function using*
875 *NetworkX*. Retrieved from

876 Haklay, M., & Weber, P. (2008). Openstreetmap: User-generated street maps. *IEEE Pervasive Computing, 7*(4),
877 12-18.

878 Hwang, S., Park, M., Lee, H.-S., & Lee, S. (2016). Hybrid simulation framework for immediate facility
879 restoration planning after a catastrophic disaster. *Journal of Construction Engineering and*
880 *Management, 142*(8), 04016026.

881 Ismail, M. A., Sadiq, R., Soleymani, H. R., & Tesfamariam, S. (2011). Developing a road performance index
882 using a Bayesian belief network model. *Journal of the Franklin Institute, 348*(9), 2539-2555.

883 ISTAT, A. S. I. (2016). Istituto Nazionale di statistica.

884 Kammouh, O., Cimellaro, G. P., & Mahin, S. A. (2018). Downtime estimation and analysis of lifelines after an
885 earthquake. *Engineering Structures, 173*, 393-403. doi:<https://doi.org/10.1016/j.engstruct.2018.06.093>

886 Kammouh, O., Noori, A. Z., Cimellaro, G. P., & Mahin, S. A. (2019). Resilience Assessment of Urban
887 Communities. *ASCE-ASME Journal of Risk and Uncertainty in Engineering Systems, Part A: Civil*
888 *Engineering, 5*(1), 04019002. doi:doi:10.1061/AJRUA6.0001004

889 Kammouh, O., Noori, A. Z., Taurino, V., Mahin, S. A., & Cimellaro, G. P. (2018). Deterministic and fuzzy-
890 based methods to evaluate community resilience. *Earthquake Engineering and Engineering Vibration,*
891 *17*(2), 261-275. doi:10.1007/s11803-018-0440-2

892 Karakoc, D. B., Barker, K., Zobel, C. W., & Almoghathawi, Y. (2020). Social Vulnerability and Equity
893 Perspectives on Interdependent Infrastructure Network Component Importance. *Sustainable Cities and*
894 *Society, 102072*.

895 Kirk, D. (2007). *NVIDIA CUDA software and GPU parallel computing architecture*. Paper presented at the
896 ISMM.

897 Latora, V., & Marchiori, M. (2001). Efficient behavior of small-world networks. *Physical review letters, 87*(19),
898 198701.

899 Liaw, A., & Wiener, M. (2002). Classification and regression by randomForest. *R news, 2*(3), 18-22.

900 Lu, X., & Guan, H. (2017). *Earthquake disaster simulation of civil infrastructures*: Springer.

901 Maguire, D. J. (1991). An overview and definition of GIS. *Geographical information systems: Principles and*
902 *applications, 1*, 9-20.

903 Marasco, S., Noori, A. Z., & Cimellaro, G. P. (2017). Resilience Assessment for the Built Environment of a
904 Virtual City. *compdyn 2017 Proceedings*, 1-13.

905 Martí, J. R. (2014). Multisystem simulation: analysis of critical infrastructures for disaster response *Networks of*
906 *networks: the last frontier of complexity* (pp. 255-277): Springer.

907 Mazzoni, S., McKenna, F., Scott, M. H., & Fenves, G. L. (2006). OpenSees command language manual. *Pacific*
908 *Earthquake Engineering Research (PEER) Center, 264*.

909 Mirza, S. A., & MacGregor, J. G. (1979). Variability of mechanical properties of reinforcing bars. *Journal of the*
910 *Structural Division*, 105(ASCE 14590 Proceeding).

911 Ni, K. S., & Nguyen, T. Q. (2009). An adaptable k -nearest neighbors algorithm for MMSE image
912 interpolation. *IEEE transactions on image processing*, 18(9), 1976-1987.

913 Noori, A. Z., Marasco, S., Kammouh, O., Domaneschi, M., & Cimellaro, G. (2017). *Smart cities to improve*
914 *resilience of communities*. Paper presented at the 8th International Conference on Structural Health
915 Monitoring of Intelligent Infrastructure.

916 Ouyang, M. (2014). Review on modeling and simulation of interdependent critical infrastructure systems.
917 *Reliability engineering & System safety*, 121, 43-60.

918 Pamungkas, A., Bekessy, S. A., & Lane, R. (2014). Vulnerability modelling to improve assessment process on
919 community vulnerability. *Procedia-Social and Behavioral Sciences*, 135, 159-166.

920 Piegsl, L. A., & Tiller, W. (2002). Algorithm for finding all k nearest neighbors. *Computer-Aided Design*, 34(2),
921 167-172.

922 Porter, K., Farokhnia, K., Cho, I., Grant, D., Jaiswal, K., Wald, D., & Noh, H. (2012). *Global vulnerability*
923 *estimation methods for the global earthquake model*. Paper presented at the 15th World Conference on
924 Earthquake Engineering, Lisbon, Portugal.

925 Prettico, G., Gangale, F., Mengolini, A., Lucas, A., & Fulli, G. (2016). Distribution System Operators
926 Observatory. *European Commission. Joint Research Centre*.

927 Renschler, C. S., Frazier, A. E., Arendt, L. A., Cimellaro, G. P., Reinhorn, A. M., & Bruneau, M. (2010). *A*
928 *framework for defining and measuring resilience at the community scale: The PEOPLES resilience*
929 *framework*: MCEER Buffalo.

930 Repetto, M. P., Burlando, M., Solari, G., De Gaetano, P., & Pizzo, M. (2017). Integrated tools for improving the
931 resilience of seaports under extreme wind events. *Sustainable Cities and Society*, 32, 277-294.

932 Ribeiro, P. J. G., & Gonçalves, L. (2019). Urban resilience: A conceptual framework. *Sustainable Cities and*
933 *Society*, 101625.

934 Rossman, L. A. (2000). EPANET 2: users manual.

935 Silva, V., Crowley, H., Pagani, M., Monelli, D., & Pinho, R. (2014). Development of the OpenQuake engine, the
936 Global Earthquake Model's open-source software for seismic risk assessment. *Natural Hazards*, 72(3),
937 1409-1427.

938 Svennerberg, G. (2010). *Beginning Google Maps API 3*: Apress.

939 Takeda, T., Sozen, M. A., & Nielsen, N. N. (1970). Reinforced concrete response to simulated earthquakes.
940 *Journal of the Structural Division*, 96(12), 2557-2573.

941 Taurino, V., Kammouh, O., Cardoni, A., & Paolo, G. (2018). RESILIENCE ASSESSMENT OF LARGE SCALE
942 WATER DISTRIBUTION NETWORKS: A SIMULATION APPROACH.

943 UnityTechnologies. (2020). Unity. Retrieved from <https://unity.com/>

944 Vrouwenvelder, T., & Faber, M. (2001). Probabilistic model code. *Joint Committee on Structural Safety, website*
945 <http://www.jcss.ethz>.

946 Walker, B., & Salt, D. (2006). The system rules: creating a mind space for resilience thinking. *Walker, B. and*
947 *Salt, D. Resilience Thinking: Sustaining Ecosystems and People in a Changing World*. Island Press,
948 Washington, 28-52.

949 Yang, Y., Ng, S. T., Zhou, S., Xu, F. J., & Li, H. (2019). Physics-based resilience assessment of interdependent
950 civil infrastructure systems with condition-varying components: A case with stormwater drainage
951 system and road transport system. *Sustainable Cities and Society*, 101886.

952 Yao, B., Khosla, A., & Fei-Fei, L. (2011). *Combining randomization and discrimination for fine-grained image*
953 *categorization*. Paper presented at the CVPR 2011.

954 Zhu, M., McKenna, F., & Scott, M. H. (2018). OpenSeesPy: Python library for the OpenSees finite element
955 framework. *SoftwareX*, 7, 6-11.

956